1 **Cellular electron tomography of the apical complex in the apicomplexan**

2 **parasite *Eimeria tenella* shows a highly organised gateway for regulated**

3 **secretion.**

4 Alana Burrell[1,2], Virginia Marugan-Hernandez[1], Flavia Moreira-Leite[2], David J P Ferguson[2], Fiona M

5 Tomley[1*], Sue Vaughan[2*]

6

7 1 The Royal Veterinary College. University of London. Hawkshead Lane, North Mymms, AL9 7TA, UK

8 2 Department of Biological and Medical Sciences. Oxford Brookes University. Gipsy Lane, Oxford,

9 OX3 0BP, UK

10

11 *Joint corresponding author

12

13 **Abstract:**

14 The apical complex of apicomplexan parasites is essential for host cell invasion and

15 intracellular survival and as the site of regulated exocytosis from specialised secretory organelles

16 called rhoptries and micronemes. Despite its importance, there is little data on the three-

17 dimensional organisation and quantification of these organelles within the apical complex or how

18 they are trafficked to this specialised region of plasma membrane for exocytosis. In coccidian

19 apicomplexans there is an additional tubulin-containing hollow barrel structure, the conoid, which

20 provides a structural gateway for this specialised secretion. Using a combination of cellular electron

21 tomography and serial block face-scanning electron microscopy (SBF-SEM) we have reconstructed

22 the entire apical end of *Eimeria tenella* sporozoites. We discovered that conoid fibre number varied,

23 but there was a fixed spacing between fibres, leading to conoids of different sizes. Associated apical

24 structures varied in size to accommodate a larger or smaller conoid diameter. However, the number

25 of subpellicular microtubules on the apical polar ring surrounding the conoid did not vary, suggesting

26 a control of apical complex size. We quantified the number and location of rhoptries and

27 micronemes within cells and show a highly organised gateway for trafficking and docking of

28 rhoptries, micronemes and vesicles within the conoid around a set of intra-conoidal microtubules.

29 Finally, we provide ultrastructural evidence for fusion of rhoptries directly through the parasite

30 plasma membrane early in infection and the presence of a pore in the parasitophorous vacuole

31 membrane, providing a structural explanation for how rhoptry proteins (ROPs) may be trafficked

32 between the parasite and the host cytoplasm.

33

34

35

## Significance:

36

37    Apicomplexan parasites cause a wide range of human and animal diseases. The apical
38    complex is essential for motility, host cell invasion and intracellular survival within a specialised
39    vacuole called the parasitophorous vacuole. We know that molecules important for all of these
40    processes are secreted from the apical complex via a set of secretory organelles and there is even
41    evidence that some parasite molecules can enter the host cell from the parasitohorous vacuole, but
42    there is little understanding of exactly how this occurs.  Here we have used three dimensional
43    electron microscopy to reconstruct the entire apical end of the parasite and whole individual
44    parasites. Our results provide important insights into the structural organisation and mechanisms for
45    delivery of parasite molecules via this important area of the cell.

46

47    **Keywords:** Apicomplexa, *Eimeria*, conoid, *Toxoplasma*.

48

49    ## Introduction:

50    A defining feature of apicomplexan parasites is the apical complex after which the phylum is
51    named. This comprises an apical polar ring to which are attached a set of helically arrayed
52    subpellicular microtubules, and two types of specialised secretory apical organelles called
53    micronemes and rhoptries that are part of the parasite endomembrane system. The Coccidia sub-
54    class of Apicomplexa, which includes the genera *Eimeria*, *Neospora*, *Sarcocystis* and *Toxoplasma*,
55    also possess a conoid, an apical cone-like hollow structure composed of tubulin-containing fibres
56    (Morrissette and Sibley, 2002) associated with two pre-conoidal rings and a pair of intra-conoidal
57    microtubules (Nichols and Chiappino, 1987). Transmission electron microscopy analysis in
58    *Toxoplasma gondii* estimated the conoid to contain ~14 tubulin fibres (Hu et al., 2002), but there
59    was a level of uncertainty in this number due to inherent difficulties in analysing such a complex
60    structure using two-dimensional methods. The two pre-conoidal rings are located at the apical tip of
61    the cell, above the conoid and just under the plasma membrane, and these rings move together with
62    the mobile conoid when it is extended in *T. gondii*, although their precise role is not understood
63    (Nichols and Chiappino, 1987; Katris et al., 2014).
64    Co-ordinated exocytosis of apical secretory organelles during host cell invasion is essential
65    not only for parasite entry into the host cell, but also for intracellular survival. Micronemes secrete
66    adhesin complexes (MICs) onto the parasite surface where they span the parasite plasma membrane
67    (PM) and connect to a parasite actinomyosin-based motility system, the glideosome, which occupies
68    a space in the parasite pellicle between the PM and the inner membrane complex for parasite

69    motility in extracellular parasites (Frénal et al., 2017). Surface exposure of MICs is essential for

70    attachment to host cells, gliding motility, migration across tissues and for the formation of a moving

71    junction (MJ) between the parasite and the host cell, during invasion (Carruthers and Tomley, 2008).

72    A complex of rhoptry neck proteins (RONs) are inserted into the host cell PM and act as cognate

73    receptors for the MIC protein AMA1, which is itself anchored to the parasite apical surface after

74    secretion. The AMA1-RON2 interaction is critical for the formation of a stable moving junction

75    (Lamarque et al., 2011) and the RON complex recruits host cytoskeletal structures to the cytosolic

76    face of the host PM, to solidify host-parasite bridging as invasion progresses (Guérin et al., 2017).

77    The MJ also sieves and removes GPI-anchored proteins from the host PM so that the newly formed

78    parasitophorous vacuole (PV) can resist endosome fusion and lysosomal destruction (Mordue et al.,

79    1999). Secreted rhoptry bulb proteins (ROPs) and membranous material contribute to the formation

80    and remodelling of the PV and its membrane and some ROPs traffic beyond the PV into the host cell

81    cytoplasm (Bradley and Sibley, 2007).

82    Secretion of both rhoptry and microneme proteins occurs from the apical complex, but the precise

83    organisation of these trafficking events is not well understood. MIC secretion from micronemes

84    occurs from the apical pole when parasites contact host cells (Frénal et al., 2017; Bumstead and

85    Tomley, 2000). This contact activates a parasite cGMP signalling pathway with two effector arms.

86    Inositol triphosphate (IP3) stimulates intracellular calcium release activating calcium-dependent

87    protein kinases (CDPKs) at the parasite apex. CDPKs then phosphorylate proteins involved in

88    microneme exocytosis and in the activation of the glideosome (Dunn et al., 1996).  Diacylglycerol

89    (DAG) is converted to phosphatic acid at the inner leaflet of the parasite PM and sensed by a

90    pleckstrin homology domain protein (APH) that lies on the surface of apical micronemes (Bullen et

91    al., 2019). Despite these advances in understanding the signalling pathway, the actual mechanism of

92    microneme exocytosis remains enigmatic. RON/ROP secretion from rhoptries also occurs at the

93    apical pole, but apart from needing previous MIC discharge (Kessler et al., 2008) little is known about

94    the signalling pathway triggering rhoptry discharge. Apical positioning of the rhoptry seems to be

95    prerequisite for RON/ROP exocytosis (Frénal et al., 2013) and it is not possible to trigger RON/ROP

96    secretion in extracellular parasites. However invasion is not essential; if actin polymerisation (and

97    invasion) are disrupted by treatment with cytochalasin D parasites are still able to attach, form a

98    tight junction with the host PM and discharge rhoptry content into nascent parasitophorous

99    'evacuoles', which can be readily detected with anti-ROP antibodies (Håkansson et al., 2001). Indeed

100   it appears that in normal *in vitro* and *in vivo* infections a proportion of host cells are injected with

101   rhoptry proteins without becoming infected; the reason for this is unknown (Koshy et al., 2012).

102   After discharge, rhoptries are occasionally seen as empty sacs (Lebrun et al., 2005) and in

3

103  intracellular parasites one or two rhoptries may be seen with their necks extending into the conoid
104  reaching the apical PM, suggesting they are anchored here and ready for secretion (Paredes-Santos
105  et al., 2012). The two intra-conoidal microtubules and associated secretory vesicles are proposed to
106  be involved in microneme and rhoptry spatial organisation within the conoid, but optical resolution
107  has been insufficient to confirm this hypothesis. Recently, a number of molecules involved in rhoptry
108  discharge have been identified, including orthologues of *Plasmodium* non-discharge rosette
109  complexes, as well as rhoptry apical surface proteins (Suarez et al., 2019) and calcium-sensing ferlins
110  (Coleman et al., 2018). While these molecules may hold the key to signalling, the key mechanisms of
111  rhoptry exocytosis, whereby RONs and ROPs cross both the parasite and the host PMs, remain
112  mysterious. The discharge of rhoptry and microneme proteins occur at the apical end presumably by
113  fusion with the PM overlying the conoid (Bannister et al., 2003; Scholtyseck and Mehlhorn, 1970),
114  but this is not well understood and there is uncertainty as to the machinery involved in fusion prior
115  to release. A recent study using cryo-electron tomography of *Toxoplasma gondii* tachyzoites showed
116  rhoptries connected to an apical vesicle underlying the plasma membrane of the conoid and a
117  rosette of non-discharge proteins embedded in the parasite plasma membrane, which appears to
118  represent machinery at least in part required for fusion and delivery of rhoptry contents into the
119  host cytosol (Aquilini et al., 2021).

120      Rhoptries have been visualised within the conoid in many studies (Dos Santos Pacheco et al.,
121  2020), but there has been some uncertainty over the precise location of micronemes either within
122  the conoid (Dubois and Soldati-Favre, 2019) or at the base of the conoid when it is protruded
123  (Paredes-Santos et al., 2012). Here, we used high resolution cellular electron tomography to
124  reconstruct the apical complex of *Eimeria tenella* sporozoites. Data from serial electron microscopy
125  tomography and serial block-face scanning electron microscopy (SBF-SEM) were combined to
126  produce 3D models showing how secretory organelles are arranged for exocytosis. Our data provide
127  evidence for fusion of the rhoptry membrane with the parasite membrane overlying the conoid and
128  a pore in the parasitophorous vacuole membrane that may be important in the delivery of rhoptry
129  contents to the host cytosol early in infection.

130
131  **Results:**
132  **Cellular electron tomography of the apical complex reveals a highly ordered**
133  **gateway for secretion.**
134      To investigate the detailed ultrastructure of the conoid and how the secretory organelles are
135  organised in the apical complex, serial section electron tomography was performed on freshly

4

136     hatched extracelluar sporozoites and invaded sporozoites (N=17, serial dual axis serial tomograms).

137     These tomograms encompassed the entire apical end covering ~2.5 μm³. Segmentation of the

138     conoid and associated structures were carried out for each serial tomogram (e.g. Movie 1 and

139     selected slices through a serial section tomogram images in Fig. 1C). Due to the complexity of the

140     overall structure, we divided the apical complex in two parts: the structures/organelles that

141     surround the conoid barrel are referred to as the 'outer' conoid components (Fig 1A) and the

142     structures/organelles contained within the barrel of the conoid are called 'inner' conoid components

143     (Fig 1B). The outer apical complex includes an electron-opaque apical polar ring (APR) (Fig 1A;

144     orange). Our work confirms that there are 24 evenly spaced subpellicular microtubules (Fig 1A;

145     green) radiating from APR and extending towards the posterior of the cell, as identified in all 17

146     tomograms. Two ring-shaped structures distal to the conoid - known as pre-conoidal ring-1 (PCR-1)

147     (Fig 1A, light blue) and pre-conoidal ring 2 (PCR-2) (Fig 1A, red) - complete the outer conoid

148     components. The outer apical complex is enclosed by the plasmalemma and partially enclosed by

149     the inner membrane complex (IMC), which is interrupted apically to form a circular apical opening

150     (not shown in the tomograms). This is located distal to the apical polar ring (APR).

151          The inner apical complex components comprise a pair of centrally located intra-conoidal

152     microtubules (Fig 1B; pink). We discovered that one of these microtubules starts and terminates in

153     line with the height of the conoid, whilst the other extends into the cell interior past the base of the

154     conoid and beyond the region covered in our tomograms, which has not been reported previously

155     (Fig 1B; pink, 1C:10 – arrows, 1C:11). Spherical vesicles of varying number are closely associated with

156     the two intra-conoidal microtubules and appear as a row of electron-opaque spheres leading

157     posteriorly from each conoid (Fig 1B – yellow; 1C: 11 - asterisks). Spherical vesicles have been

158     identified in this configuration in numerous studies, but the composition of these are unknown

159     (Paredes-Santos et al., 2012). There has been some uncertainty over the presence or absence of

160     microneme trafficking into the conoid barrel in *Toxoplasma gondii* (Dubois and Soldati-Favre, 2019),

161     but our tomograms clearly show both rhoptries (Fig 1B, dark blue; 1C: 7,8 - "R") and micronemes (Fig

162     1B, light green; 1C: 10 - "M") located within the conoid area of all 17 tomograms (see below, movie

163     1, Supple. Fig 2).

164          When viewed as a three-dimensional reconstruction, the conoid appears as an open

165     truncated cone formed from closely apposed helical fibres which follow a left-handed helical path

166     towards the apical end of the parasite (Fig 1A; white). Quantification of the size of the conoid and

167     the number of tubulin-containing fibres reveals a variation in fibre number between individual

168     parasites, but in all tomograms there were always 24 evenly spaced subpellicular microtubules

169     connected to the apical polar ring that surrounds the conoid. Negatively stained whole-mount

170    cytoskeletons of *T. gondii* estimates that the conoid is composed of ~14 helically arranged tubulin-

171    containing fibers (Hu et al., 2002), but high resolution tomography of the conoid had not been

172    carried out to confirm this. Our high-resolution tomograms show that there are between 13 and 16

173    fibres in the conoid, and there can be variation in fibre number even in genetically identical

174    sporozoites within the same sporocyst (Shirley and Harvey, 1996) (Supple. Fig. 1A). The width of

175    each conoid fibre was constant at 22 ± 2 nm and the spacing between each conoid fibre also

176    remained constant at 33 nm ± 4 nm irrespective of conoid fiber number (supple. Fig 1B). This fixed

177    arrangement of fibre width and distance between each fibre means that a conoid with more fibres

178    must have a larger diameter (Supple. Fig 1C). This was confirmed by measurements of the conoid

179    diameter at the base (mean = 340 nm, +/-20 nm SD) and correlated with fibre number, which

180    revealed a positive correlation (coefficient = 0.78, p = 0.014, Pearson correlation).

181         Further quantitative analysis of the relationship between the increasing conoid diameter

182    and the size of other apical structures was carried out. There was no correlation between conoid

183    height (mean = 193 nm, +/- 35 nm SD) and fibre number (coefficient = 0.57, p=0.113, Pearson

184    correlation), suggesting that differences in fibre number are not linked the length of the conoid

185    fibres (Supple. Fig 1C). The conoid diameter did correlate to the diameter of the pre-conoidal rings.

186    PCR-1 diameter was 169.3 nm (+/- 9.6 nm) and PCR-2 diameter was 221.5 nm (+/- 14.5 nm) and the

187    increase in diameter of both rings was correlated with increasing conoid base diameter (PCR-1;

188    Pearson correlation, r = 0.97, p<0.001; PCR-2; Pearson correlation, r = 0.74, p = 0.037). Finally, APR

189    diameter was 393nm (+/- 19 nm) and there was also a positive correlation between APR diameter

190    and conoid base diameter (= 0.76; p = 0.017, Pearson correlation). Presumably, this would be

191    important in order to maintain the distance between the APR and conoid (Supple. Fig 1D). In

192    summary, our measurements reveal there are differences in conoid fibre number resulting in

193    dependency relationships between the size of the conoid and outer conoid components in order to

194    maintain the integrity of the overall structure despite size heterogeneity between individual

195    parasites.

196

197    **Micronemes and rhoptries are organised along the intra-conoidal**

198    **microtubules and closely associated with the plasma membrane overlying**

199    **the conoid.**

200         The serial tomograms we generated encompassed the full area of the conoid in enough

201    resolution to allow us to establish the precise location and number of each type of secretory

202    organelle. Although microneme proteins are known to be secreted at the apical pole, the precise

6

203  location and mechanism of trafficking of microneme proteins into the apical complex is uncertain
204  and a detailed quantitative analysis had not been carried out previously. In our dataset set we
205  discovered 1-2 rhoptries, 1-5 micronemes and 1-3 spherical vesicles within the barrel of the conoid
206  in all tomograms (Fig 2A-D, Fig 1L, M). Supple. Fig 2 shows examples of 5 freshly excysted
207  sporozoites with differing number of micronemes within the conoid area and entering the conoid
208  area. In addition, rhoptries, micronemes and spherical vesicles were always closely associated with
209  intra-conoidal microtubules, which are located centrally within the barrel of the conoid (Fig 1B, 2A,
210  Movie 1). To quantify the spatial relationships between the intra-conoidal microtubule pair and
211  micronemes, rhoptries and spherical vesicles, we measured the distances between each organelle
212  and the intra-conoidal microtubules, and between each organelle and the conoid fibres (Fig 2C - G).
213  One of the organelles were chosen in each tomogram and measurements taken at roughly the same
214  position within the conoid to take account of the cone shape of the conoid. These measurements
215  reveal that micronemes, rhoptries and spherical vesicles are always located significantly closer to the
216  intra-conoidal microtubule pair within the central barrel of the conoid than to the fibres of the
217  conoid barrel (Fig 2E-G), suggesting a potential role for the intra-conoidal microtubules in organising
218  the secretory organelles within the conoid in readiness for secretion. The plasma membrane
219  overlying the conoid was checked for evidence of fusion events or close apposition of microneme,
220  rhoptry or spherical vesicle membranes. All rhoptries within the conoid were in close apposition with
221  the plasma membrane. Spherical vesicles were organised in single file along the intra-conoidal
222  microtubules and there were always 1 or 2 micronemes and at least 1 spherical vesicle located in
223  close apposition with the plasma membrane overlying the conoid, as well as being closely associated
224  with the intra-conoidal microtubules (Fig 2H-O). This suggests there is a sequential trafficking of
225  micronemes and spherical vesicles along the intra-conoidal microtubules to the plasma membrane
226  overlying the conoid, in preparation for secretion.

227  Whilst fusion of microneme or spherical vesicle membranes with the plasma membrane was
228  not observed in freshly excysted sporozoites, our dataset included two serial section dual-axis
229  tomograms of sporozoites situated within a parasitophorous vacuole (PV) after sporozoite invasion
230  of Madin-Darby bovine kidney (MDBK) cells. In one of these invaded sporozoite tomograms fixed at
231  30 min post-infection, a rhoptry was identified with an electron-lucent interior instead of the usual
232  electron dense rhoptry organisation (Fig 3A and inset, B and inset; Movie 2). The electron-lucent
233  rhoptry (ELR) differed in shape from the electron dense rhoptries (R) in the same and other
234  tomograms, having a broader base and flask-shaped (Fig 3C). Intriguingly, the electron-lucent
235  rhoptry appeared to be continuous with the parasite plasma membrane as if the rhoptry had fused
236  with the parasite plasma membrane overlying the conoid, to release its contents (Fig 3B and inset).

237    At the point of fusion there was a hole in the PV membrane (PVM) appearing to create a channel

238    passing through both the parasite plasma membrane and the PVM, connecting the electron-lucent

239    rhoptry directly with host cell cytoplasm (Fig 3B and inset, C, D, Movie 2).

240    Overall, our extensive tomography analysis of both freshly excysted and invaded sporozoites

241    revealed that different types of secretory organelles converge within the conoid and are closely

242    associated with the intra-conoidalal microtubules, forming what appears to be a highly ordered

243    secretory gateway at the apical end of the cell.

244

## Whole cell reconstructions of individual sporozoites reveals the organisation and location of major sporozoite organelles.

247    Our tomography data revealed that only a limited number of individual secretory organelles

248    are located within the conoid area, yet many studies show the presence of hundreds of micronemes

249    within the apical end of the parasite outside the conoid area. To better understand the broad

250    localisation and number of secretory organelles, freshly excysted sporozoites were prepared for

251    serial block face-scanning electron microscopy (SBF-SEM), which allows automated collection of

252    datasets containing hundreds of sequential serial sections. A total of 25 whole individual sporozoite

253    cells found in aligned SBF-SEM series were reconstructed and analysed for organelle number and

254    three dimensional organisation. A single slice of a freshly excysted sporozoite illustrates that most

255    major organelles were visible by SBF-SEM (Fig 4A, B, C; modelled in 4F). Movie 3 illustrates a portion

256    of the SBF-SEM dataset showing 25 slices containing a sporozoite. Organelle volume and number

257    were determined by manual segmentation of each organelle, and the relative abundance and

258    location of all identifiable organelles (including micronemes and rhoptries) were analysed (Fig 4F;

259    Suppl. Fig 3). Due to the number and close packing of micronemes located mainly at the apical end

260    of the sporozoite, it was not possible to accurately count them. Instead, micronemes were

261    segmented using a combination of pixel-density thresholding and manual area selection in three

262    whole cell volumes (Fig 4D). The total mean whole cell volume of individual sporozoites was 61.27

263    $\mu m^3$ (Supple. Fig 3A) with micronemes comprising 5% of whole cell volume and rhoptries <0.5% of

264    whole cell volume (Fig 4G). This quantitative analysis revealed that refractile bodies make up 36% of

265    whole cell volume (2 per cell in freshly excysted sporozoites), with the nucleus (1 per cell) and

266    amylopectin granules (~196/cell) each comprising 4%, mitochondria (~14/cell) 2% and

267    acidocalcisomes (~13/cell) 1% of whole cell volume (Supple. Fig 3 for full quantification). The

268    majority of micronemes were densely packed at the apical end of the sporozoite (Fig 3D). Rhoptries

8

269    were observed as club-shaped structures with a rounded 'bulb' region and an elongated 'neck'
270    region. They were also mostly found towards the sporozoite apical end, although some rhoptries
271    were present in the central and posterior parts of the cell (Fig 4E). Unfortunately, the spherical
272    vesicles observed by tomography (in association with the intra-conoidal microtubules, e.g Fig 1B)
273    were not clearly identified in the reconstructed whole cell SBF-SEM data.  By combining findings
274    from tomography and SBF-SEM, we conclude that *E. tenella* sporozoites contain an abundance of
275    micronemes and rhoptries, and only a small number of these are seen within the conoid where
276    secretion occurs, suggesting that there is significant directed movement of these secretory
277    organelles converging at the conoid.

278

279    **Discussion:**

280    Secretion of microneme and rhoptry contents from the apical end of apicomplexan zoites is
281    well documented and hundreds of micronemes have been visualised closely packed at the apical end
282    of many different apicomplexan parasites by classic transmission electron microscopy (TEM) thin
283    sections  (For review see Dubois and Soldati-Favre, 2019). Exactly how micronemes are trafficked for
284    secretion to this small portion of plasma membrane is not well understood. In *T. gondii*, focussed ion
285    beam scanning electron microscopy (FIB-SEM) images did not find micronemes within the conoid
286    area and  it was  proposed that microneme secretion could occur adjacent to the conoid, close to
287    APR and the subpellicular microtubules, where a membrane space could open up as the conoid
288    protrudes (Paredes-Santos et al., 2012), rather than secretion occurring at the plasma membrane
289    directly overlying the conoid. However, further studies using the same technique did observe a
290    microneme inside the conoid area. Although the intra-conoidal microtubules could not be resolved
291    by FIB-SEM (Dubois and Soldati-Favre, 2019), they have been proposed to be involved in secretory
292    cargo trafficking (Hu et al., 2006b). Our experimental data using high resolution cellular electron
293    tomography in *E. tenella* provide experimental evidence for the role of the intra-conoidal
294    microtubules in the trafficking of micronemes through the conoid to the plasma membrane
295    overlying the conoid, suggesting an orderly system for transporting these organelles to the
296    membrane in preparation for docking, fusion and release of contents. We also show here that
297    rhoptries and a set of spherical vesicles (of yet unknown composition) are also closely associated
298    with the intra-conoidal microtubules. This suggests that the intra-conoidal microtubules are a major
299    organiser of orderly trafficking within the conoid area. In addition, our tomograms show that at least
300    one intra-conoidal microtubule may be involved in trafficking of organelles into the conoid space,
301    because this microtubule extends posteriorly into the cytoplasm (beyond the region covered by our

302    tomograms), where it is ideally positioned to interact with secretory organelles and 'guide' them to

303    the conoid for discharge.

304    Careful analysis of tomograms did not find direct evidence of fusion of microneme or

305    spherical vesicle membranes with the plasma membrane overlying the conoid, despite their close

306    proximity to the plasma membrane in nearly all tomograms. This might be due to the fixation

307    method used in this study or could indicate that the process is very fast and therefore extremely

308    difficult to capture in still images, but certainly the signalling cascade for membrane fusion exists in

309    apicomplexan organisms (for review see (Dubois and Soldati-Favre, 2019). Our observation of an

310    apparent fusion of a rhoptry to the parasite plasma membrane overlying the conoid and a small pore

311    in the parasitophorous vacuole membrane surrounding an invaded sporozoite has significant

312    implications in re-shaping what is understood about the parasitophorous vacuole. The current view

313    of the apicomplexan parasitophorous vacuole membrane is that this is sealed, requiring insertion of

314    parasite-derived pores for the transport of molecules between the host cell cytosol and the

315    parasitophorous intra-vacuolar space, and in particular for the trafficking of rhoptry proteins into the

316    host cytosol (Gold et al., 2015; Marino et al., 2018). However, our data as well as a rare thin section

317    electron microscopy of an invaded *T. gondii* tachyzoite show a direct connection or pore linking an

318    electron-lucent rhoptry and the host cell cytosol (Nichols et al., 1983). Recently, a mechanism

319    proposed to be involved upstream of rhoptry fusion was discovered in *T. gondii* tachyzoites using

320    cryo-electron tomography. The authors showed that rhoptries connected with an apical vesicle

321    underlying the plasma membrane of the conoid and the position of the apical vesicle coincided with

322    a rosette of non-discharge proteins embedded in the parasite plasma membrane. Direct fusion and a

323    pore were not observed in this study as we show in this work, but the formation of a rosette

324    containing non-discharge proteins maybe a pre-requisite for fusion of membranes and release of

325    rhoptry proteins (Aquilini et al., 2021). It is probable that rhoptry fusion is a highly dynamic event

326    that takes place only at specific stages of intracellular infection, which might explain why they have

327    been visualised only on rare occasions. In addition the pore is small (~40nm), which would make it

328    even more difficult to obtain clear images by thin section transmission electron microscopy.

329    Our detailed measurements and quantification of the conoid showed a highly ordered

330    organisation of conoid fibres in a left-handed helical organisation with fixed spacing between the

331    fibres. This is the first detailed high resolution three dimensional reconstruction of a coccidian

332    conoid and interestingly we have shown there is heterogeneity in fibre number between individual

333    sporozoites even at different developmental stages. This difference in fibre number influences the

334    overall size of the conoid and directly correlates with the associated diameters of the two conoidal

335    rings and the APR, presumably to ensure overall structural integrity to allow for conoid mobility, so it

336 can be recessed and flushed with the apical polar ring or extruded beyond the apical polar ring

337 (Monteiro et al., 2001). Intriguingly in all parasites there were always 24 subpellicular microtubules

338 on the APR, which presumably places a physical constraint for the minimum and maximum possible

339 diameter of the APR and its associated structures and thus, dictates the minimum and maximum

340 overall dimensions of the apical complex at least in the sporozoite stage of the parasite.

341 Here we show that combining high resolution cellular electron tomography and lower

342 resolution SBF-SEM data is a powerful way of investigating specific areas of cells with a whole cell

343 view. These datasets reveal a highly organised gateway for trafficking of secretory organelles to the

344 conoid area of the apical complex. Further work will be required to understand the role of rhoptry

345 fusion and pore formation within the PV and how individual micronemes are trafficked into the

346 conoid area from such a large cluster underlying the conoid area.

354 **Figure legends:**

355 **Figure 1: Components of the apical complex in sporozoites of _E. tenella_.** The apical complex is

356 divided into outer conoid (A) and inner conoid (B) components. A and B: Segmentation from

357 tomogram. Outer conoid components; Conoid fibres (white); 2 pre-conoidal rings (PCR 1 and 2) (light

358 blue and red), apical polar ring (gold) in association with sub-pellicular microtubules (green); B: Inner

359 conoid components, rhoptry (dark blue), microneme (light green), secretory vesicle (yellow), intra-

360 conoidal microtubule pair (pink); Scale bars - 200nm. C: Series of 15 tomographic slices through a

361 representative tomogram, conoid – yellow arrowheads, micronemes – arrows throughout the series,

362 microneme within the conoid (10,11), Rhoptry (7, 8), long and short intra-conoidal microtubules

363 (10), spherical vesicle asterisks (11), Conoid fibres and inset (13). Scale bar - 500nm.

364

365 **Figure 2: Secretory organelles and their association with the intra-conoidal microtubules and**

366 **overlying the plasma membrane.** A: Series of rotational views of a segmentation created from one

367 serial tomogram illustrating the spatial grouping and alignment of microneme (light blue), rhoptries

368 (dark blue) and spherical vesicles (yellow) with the intra-conoidal microtubule pair (pink); B:

369 Segmentation of a serial tomogram illustrating the relative positioning of the microneme (light

11

370    green), rhoptry (dark blue) and spherical vesicles (yellow) with the apical end of the parasite; C and

371    D: slices taken from different tomograms (C) longitudinal view and (D) cross section view illustrating

372    how measurements were taken showing the distances from a microneme (M), rhoptry (R) and

373    spherical vesicle (SV) to either the intra-conoidal microtubules or conoid. Double-headed red arrows

374    show where the measurements were taken, single arrow in C for location of the conoid. Single arrow

375    in D the location of intra-conoidal microtubules; E-G: Micronemes, spherical vesicles and rhoptries

376    were significantly closer to the intra-conoidal microtubules (IM) than to the conoid (C) (t-test, p <

377    0.0001) (N= 17); H - I: Longitudinal slice views from 8 tomograms illustrating a spherical vesicle (red

378    arrows), microneme (blue arrows and black arrowheads) in close association with the plasma

379    membrane overlying the conoid in each tomogram. Yellow arrowheads show the outer edge of the

380    conoid in each example. Scale bars – 100nm.

381

382    **Figure 3: Characterisation of an electron lucent rhoptry in an intracellular sporozoite.** A: Slice from

383    a tomogram illustrating an intracellular sporozoite with an electron lucent rhoptry (box and A: inset)

384    close to a host cell nucleus (30 min post-infection sample) scale bar 1µm; A: inset: Higher

385    magnification of A illustrating the electron lucent rhoptry (ELR) at the conoid (white arrowheads

386    point out the boundaries of the conoid). Scale bar 500nm; B and B: inset: Slice from a tomogram

387    showing the electron lucent 'empty' rhoptry (ELR) which appeared to be continuous with the

388    parasite plasma membrane and attached at its apex to a hole in the parasitophorous membrane

389    creating a channel passing through both the parasite plasma membrane and the PVM connecting the

390    'empty rhoptry' directly with host cell cytoplasm B – scale bar 100nm; B inset scale bar 50nm;  C and

391    D: Segmentation of a serial tomogram outlined in A and B  to illustrate the three dimensional

392    organisation and relative positioning of the electron lucent rhoptry (ELR – dark blue), electron dense

393    rhoptry (R – dark blue), conoid fibres (white), spherical vesicles (yellow), parasite plasma membrane

394    (purple), parasitophorous vacuole membrane (green), PCR-1 and 2 (light blue and red), subpellicular

395    microtubules (yellow), intra-conoidal microtubules (pink).

396

397    **Figure 4: SBF-SEM quantification of micronemes, rhoptries and other major organelles in freshly**

398    **excysted sporozoites.** A: Longitudinal section from an SBF-SEM dataset illustrating the major

399    organelles. B and C: Additional slices from SBF-SEM datasets to illustrate identification of major

400    organelles. D and E: Quantification and location of microneme and rhoptry organelles in SBF-SEM

401    whole cell reconstructions.    F. Combined model illustrating the positioning of all the major

402    organelles: micronemes – yellow, refractile bodies – green, amylopectin granules – red,

403    acidocalcisomes – black, rhoptries – purple, nucleus – blue - Scale bars – 1µm; G. Relative volumes of

404    major organelles in freshly excysted sporozoites.

405

406    **Supplemental figure 1: Conoid fibre number variation in sporozoites from pre-excystation**

407    **sporocysts, freshly excysted and intracellular.** A: Segmentation of sporozoite conoids from pre-

408    excystation sporozoites within sporocysts, freshly excysted and intracellular sporozoites. The

409    numbers next to sporocysts indicates matching sporozoites within a sporocyst; B: segmentation of a

410    conoid (white) illustrating how measurements were taken for conoid fibre width (1) and conoid fibre

411    to fibre spacing (2); C: segmentation of sporozoite conoid area illustrating how measurements of

412    conoid diameter and height were taken; D: segmentation of a sporozoite conoid area illustrating the

413    measurement criteria of conoid to apical polar ring (arrow). Index: Conoid fibres (white); 2 pre-

414    conoidal rings (PCR 1 and 2) (light blue and red), apical polar ring (gold) in association with sub-

415    pellicular microtubules (green).

416

417    **Supplemental figure 2:** A selected tomogram slices from 5 serial tomograms to illustrate the number

418    of micronemes (mic) and rhoptries in the conoid area. All micronemes that were either partially or

419    fully within the conoid were included. Conoid is highlighted with yellow arrowheads in all examples.

420    Tomogram A containing 2 rhoptries and 5 micronemes within the conoid. Mic 1 and 3 are closest to

421    the plasma membrane underlying the conoid. Mic 2, 4 and 5 have partially entered the conoid area;

422    Tomogram B, slices from a tomogram containing 2 rhoptries and 3 micronemes. Mic 1 is closest to

423    the plasma membrane; Tomogram C, slices from a tomogram with 2 rhoptries and 2 micronemes;

424    Tomogram D, slices from a tomogram containing 2 rhopries and 2 micronemes. Mic 1 is closest to

425    the plasma membrane; Tomogram E, slices from a tomogram containing 2 rhoptries and 2

426    micronemes.

427

428    **Supplemental figure 3: Volume and numbers of major organelles from whole cell reconstructions**

429    **of freshly excysted sporozoites by SBF-SEM.** Analyses was calculated from segmented SBF-SEM

430    data for each organelle in freshly excysted sporozoites. For each organelle the mean volume of an

431    individual organelle is included, SD = standard deviation, COV = co-efficient of variation, range of

432    volumes of a particular organelle or cell volume. The number of organelles per cell is included for

433    amylopectin granules, acidocalcisomes and mitochondria. AP = Apical end of the parasite. Scale bar

434    1µm.

435    **Movie 1:** Serial section cellular electron tomogram containing the apical complex of a freshly

436    excysted sporozoite and segmentation of the dataset to illustrate the three dimensional model.

13

437 Conoid fibres (white); 2 pre-conoidal rings (PCR 1 and 2) (light blue and red), apical polar ring (gold)

438 in association with sub-pellicular microtubules (green); rhoptry X 1 within the conoid (dark blue),

439 micronemes X 2 modelled within the conoid (light green), secretory vesicles (yellow), intra-conoidal

440 microtubule pair (pink);

441 **Movie 2:** Serial section cellular electron tomogram of an infected MDKB cell 30 mins post-infection

442 containing an electron lucent rhoptry and pore. Movie illustrates the tomogram data followed by the

443 segmentation. Colour scheme as per Movie 1 figure legend.

444 **Movie 3:** A total of 25 sequential slices (~100nm thick) through an SBF-SEM dataset to illustrate a

445 whole freshly excysted sporozoite used for quantitative analysis of organelles in Fig 4 and Supple. Fig

446 3.

447

448

449

450 # Methods:

451 **Infection of chickens and sporozoite purification**

452 Three-week-old Lohmann chickens (purchased from APHA Weybridge) kept under specific pathogen

453 free conditions were orally infected with 4,000 sporulated *E. tenella* Wisconsin strain oocysts

454 (Shirley, 1995). Oocysts were harvested at 7 days post-infection and excystation and sporozoite

455 purification performed as previously described (Pastor-Fernández et al., 2020).

456

457 **In vitro *E. tenella* infections**

458 The NBL-1 line of MDBK cells (ECACC-Sigma-Aldrich, Salisbury, UK) were prepared as previously

459 described (Marugan-Hernandez et al; 2020). One millilitre of cell-culture medium containing 0.35 x

460 $10^6$ MDBK cells was added to wells of a 24 well culture plate. Cells were left to settle for up to 3 hr at

461 38 °C, 5% $CO_2$, prior to infection with sporozoites. Freshly-purified sporozoites were pelleted by

462 centrifugation at ~ 600 RCF for 10 min and re-suspended in cell-culture medium at a concentration

463 of 3.5 million sporozoites per ml. One millilitre of sporozoite suspension was added to each MDBK-

464 cell containing well.

465

466 **Preparation of freshly excysted sporozoites for electron microscopy**

467 Freshly purified sporozoites (~10-50 million) were suspended in 1 ml of primary fix (2% freshly-

468 prepared formaldehyde solution (Sigma-Aldrich), 2.5% electron microscopy grade glutaraldehyde

469 (TAAB) and 0.1 M sodium cacodylate buffer (TAAB) in double distilled (dd $H_2O$). Sporozoites were left

14

470    in primary fixative for two hours at 4˚C. Fixed sporozoites were washed five times in 0.1 M

471    cacodylate buffer pH 7.4 for 10 min. Sporozoites were pelleted by centrifugation and incubated in

472    2% osmium tetroxide (TAAB) in 0.1 M cacodylate buffer for 60 min at 4˚C. For uranyl acetate

473    staining, sporozoites were added to 1 ml molten 3% agarose (2-Hydroxyethyl agarose – Sigma-

474    Aldrich, dissolved in ddH$_2$O), centrifuged and incubated at 4˚C for 5 min. Approximately 1 mm³

475    blocks were cut from the part of the agarose containing sporozoites and incubated in freshly-filtered

476    2% aqueous uranyl acetate (Agar scientific) in the dark at 4˚C overnight. Sporozoites were washed in

477    ddH20 and then dehydrated by a series of 20 min incubations in acetone/ddH$_2$0 solutions. Samples

478    were incubated for 2 hours in 25% epoxy resin (TAAB 812 resin premix kit) in acetone; overnight in

479    50% resin in acetone; 6 hrs in 75% resin in acetone; overnight in 100% resin, and finally, two changes

480    of 100% resin for 2 hours each. Polymerisation was achieved by incubation at 60°C for 24 h.

481

482

483

484    **Preparation of host cells infected with sporozoites for electron microscopy**

485    Electron microscopy grade glutaraldehyde was added to the infected MDBK cells for 15 min then

486    primary fixation carried out as above.

487

488    **Electron tomography and measurements**

489    Transmission electron tomography was performed using one of several transmission electron

490    microscopes: H-7560 (Hitachi™), Spirit (Tecnai™, FEI™/Thermo Fisher Scientific™) or Talos™

491    (FEI™/Thermo Fisher Scientific™). Sections were cut at 150 nm thickness for 120 kilovolts (kV)

492    (Hitachi™ H-7560 or Tecnai™ Spirit electron microscopes) and at 150 nm-200 nm thickness for 200

493    kV (FEI™ Talos™ electron microscope). Tomogram tilt series generated using the Hitachi™ H-7560

494    electron microscope were taken from -60˚ to +60˚ with intervals of +1˚. For tomography data

495    acquisition using the Tecnai™ Spirit electron microscope, automated centring, focus adjustment, tilt

496    setting, and image capture were performed using Xplore*3D*™ software by FEI™. For tomography

497    data acquisition using the FEI™ Talos™ electron microscope, automated centring, focus adjustment,

498    tilt setting, and image capture were performed using DigitalMicrograph™ (Gatan™) with SerialEM™

499    plug-in (Mastronarde, October 2005). Regardless of the microscope used, dual axis tomograms were

500    collected by rotating the grid by 90˚ and repeating the tilt series image collection. Tomogram image

501    data series processing, segmentation of the tomograms (modelling) to produce three dimensional

502    reconstructions and all measurements from the tomograms were also carried out using using

503 IMOD™ software (Kremer et al., 1996) (University of Colorado, Boulder). All measurements were

504 carried out in IMOD. Measurement were also carried out using the measurement features in IMOD.

505

506 **Serial block face scanning electron microscopy (SBF-SEM) image acquisition**

507 SBF-SEM data was collected using a Zeiss™ Merlin scanning electron microscope with Gatan™

508 3View™ automated sectioning and image capture system. Samples were trimmed to ~1 mm³ and

509 mounted on 3view sample pins using an epoxy conductive adhesive from Circuitworks™. After

510 insertion of the mounted block, the intra-microscope diamond-knife was advanced towards the

511 block-face by 200 nm cutting-strokes until sectioning of the block face was observed. The block-face

512 was then imaged using a scanning electron beam with 3-5 kV accelerating voltage. Electron signal

513 was detected using a back-scatter electron detector (OnPoint, Gatan) and nitrogen gas was injected

514 to raise chamber pressure to 30pa. SBF-SEM data was processed using IMOD™ software, run

515 through Cygwin™ command line interface. Segmentation was also carried out using IMOD™

516 software. (University of Colorado, Boulder).

517

518 **Statistical analysis**

519 Statistical analyses were performed using IBM™ SPSS™ version 25 software. A t-test was used to test

520 for an association between a continuous variable and a binary categorical variable where there was

521 normal distribution for both groups. If testing for an association between a continuous variable and

522 a binary categorical variable where one or both groups did not show normal distribution, the Mann-

523 Whitney U test was used. If dealing with a continuous variable and a categorical variable with more

524 than two groups, where the continuous data was normally distributed for all the groups, One-Way

525 ANOVA was used followed by a post-hoc Turkey HSD test. If there was a continuous variable and a

526 categorical variable with more than two groups, where data within at least one of the groups was

527 not normally distributed, then the Kruskal-Wallis test was used. The Chi-squared test was used when

528 assessing for a statistically significant association between two categorical variables. See individual

529 figures and legends for specific tests for each experiment.

530

531 **References:**

532 Aquilini, E., M.M. Cova, S.K. Mageswaran, N. Dos Santos Pacheco, D. Sparvoli, D.M. Penarete-Vargas,
533     R. Najm, A. Graindorge, C. Suarez, M. Maynadier, L. Berry-Sterkers, S. Urbach, P.R. Fahy, A.N.
534     Guérin, B. Striepen, J.-F. Dubremetz, Y.-W. Chang, A.P. Turkewitz, and M. Lebrun. 2021. An
535     Alveolata secretory machinery adapted to parasite host cell invasion. *Nat Microbiol*. 6:425–
536     434. doi:10.1038/s41564-020-00854-z.

537     Bannister, L.H., J.M. Hopkins, A.R. Dluzewski, G. Margos, I.T. Williams, M.J. Blackman, C.H. Kocken,
538           A.W. Thomas, and G.H. Mitchell. 2003. Plasmodium falciparum apical membrane antigen 1
539           (PfAMA-1) is translocated within micronemes along subpellicular microtubules during
540           merozoite development. *J Cell Sci*. 116:3825–3834. doi:10.1242/jcs.00665.

541     Bradley, P.J., and L.D. Sibley. 2007. Rhoptries: an arsenal of secreted virulence factors. *Curr Opin*
542           *Microbiol*. 10:582–587. doi:10.1016/j.mib.2007.09.013.

543     Bullen, H.E., H. Bisio, and D. Soldati-Favre. 2019. The triumvirate of signaling molecules controlling
544           Toxoplasma microneme exocytosis: Cyclic GMP, calcium, and phosphatidic acid. *PLoS*
545           *Pathog*. 15:e1007670. doi:10.1371/journal.ppat.1007670.

546     Bumstead, J., and F. Tomley. 2000. Induction of secretion and surface capping of microneme
547           proteins in Eimeria tenella. *Mol Biochem Parasitol*. 110:311–321. doi:10.1016/s0166-
548           6851(00)00280-2.

549     Carruthers, V.B., and F.M. Tomley. 2008. Microneme proteins in apicomplexans. *Subcell Biochem*.
550           47:33–45. doi:10.1007/978-0-387-78267-6_2.

551     Coleman, B.I., S. Saha, S. Sato, K. Engelberg, D.J.P. Ferguson, I. Coppens, M.B. Lodoen, and M.-J.
552           Gubbels. 2018. A Member of the Ferlin Calcium Sensor Family Is Essential for Toxoplasma
553           gondii Rhoptry Secretion. *mBio*. 9. doi:10.1128/mBio.01510-18.

554     Diallo, M.A., A. Sausset, A. Gnahoui-David, A.R.E. Silva, A. Brionne, Y. Le Vern, F.I. Bussière, J. Tottey,
555           S. Lacroix-Lamandé, F. Laurent, and A. Silvestre. 2019. Eimeria tenella ROP kinase EtROP1
556           induces G0/G1 cell cycle arrest and inhibits host cell apoptosis. *Cell Microbiol*. 21:e13027.
557           doi:10.1111/cmi.13027.

558     Dos Santos Pacheco, N., N. Tosetti, L. Koreny, R.F. Waller, and D. Soldati-Favre. 2020. Evolution,
559           Composition, Assembly, and Function of the Conoid in Apicomplexa. *Trends Parasitol*.
560           36:688–704. doi:10.1016/j.pt.2020.05.001.

561     Dubois, D.J., and D. Soldati-Favre. 2019. Biogenesis and secretion of micronemes in Toxoplasma
562           gondii. *Cell Microbiol*. 21:e13018. doi:10.1111/cmi.13018.

563     Dunn, P.P., J.M. Bumstead, and F.M. Tomley. 1996. Sequence, expression and localization of
564           calmodulin-domain protein kinases in Eimeria tenella and Eimeria maxima. *Parasitology*. 113
565           ( Pt 5):439–448. doi:10.1017/s0031182000081506.

566     Frénal, K., J.-F. Dubremetz, M. Lebrun, and D. Soldati-Favre. 2017. Gliding motility powers invasion
567           and egress in Apicomplexa. *Nat Rev Microbiol*. 15:645–660. doi:10.1038/nrmicro.2017.86.

568     Frénal, K., C.L. Tay, C. Mueller, E.S. Bushell, Y. Jia, A. Graindorge, O. Billker, J.C. Rayner, and D.
569           Soldati-Favre. 2013. Global analysis of apicomplexan protein S-acyl transferases reveals an
570           enzyme essential for invasion. *Traffic*. 14:895–911. doi:10.1111/tra.12081.

571     Gold, D.A., A.D. Kaplan, A. Lis, G.C.L. Bett, E.E. Rosowski, K.M. Cirelli, A. Bougdour, S.M. Sidik, J.R.
572           Beck, S. Lourido, P.F. Egea, P.J. Bradley, M.-A. Hakimi, R.L. Rasmusson, and J.P.J. Saeij. 2015.
573           The Toxoplasma Dense Granule Proteins GRA17 and GRA23 Mediate the Movement of Small
574           Molecules between the Host and the Parasitophorous Vacuole. *Cell Host Microbe*. 17:642–
575           652. doi:10.1016/j.chom.2015.04.003.

576   Guérin, A., R.M. Corrales, M.L. Parker, M.H. Lamarque, D. Jacot, H. El Hajj, D. Soldati-Favre, M.J.
577        Boulanger, and M. Lebrun. 2017. Efficient invasion by Toxoplasma depends on the
578        subversion of host protein networks. *Nat Microbiol*. 2:1358–1366. doi:10.1038/s41564-017-
579        0018-1.

580   Håkansson, S., A.J. Charron, and L.D. Sibley. 2001. Toxoplasma evacuoles: a two-step process of
581        secretion and fusion forms the parasitophorous vacuole. *EMBO J*. 20:3132–3144.
582        doi:10.1093/emboj/20.12.3132.

583   Hu, K., D.S. Roos, and J.M. Murray. 2002. A novel polymer of tubulin forms the conoid of Toxoplasma
584        gondii. *J Cell Biol*. 156:1039–1050. doi:10.1083/jcb.200112086.

585   Katris, N.J., G.G. van Dooren, P.J. McMillan, E. Hanssen, L. Tilley, and R.F. Waller. 2014. The apical
586        complex provides a regulated gateway for secretion of invasion factors in Toxoplasma. *PLoS*
587        *Pathog*. 10:e1004074. doi:10.1371/journal.ppat.1004074.

588   Kessler, H., A. Herm-Götz, S. Hegge, M. Rauch, D. Soldati-Favre, F. Frischknecht, and M. Meissner.
589        2008. Microneme protein 8--a new essential invasion factor in Toxoplasma gondii. *J Cell Sci*.
590        121:947–956. doi:10.1242/jcs.022350.

591   Koshy, A.A., H.K. Dietrich, D.A. Christian, J.H. Melehani, A.J. Shastri, C.A. Hunter, and J.C. Boothroyd.
592        2012. Toxoplasma co-opts host cells it does not invade. *PLoS Pathog*. 8:e1002825.
593        doi:10.1371/journal.ppat.1002825.

594   Kremer, J.R., D.N. Mastronarde, and J.R. McIntosh. 1996. Computer visualization of three-
595        dimensional image data using IMOD. *J Struct Biol*. 116:71–76. doi:10.1006/jsbi.1996.0013.

596   Lamarque, M., S. Besteiro, J. Papoin, M. Roques, B. Vulliez-Le Normand, J. Morlon-Guyot, J.-F.
597        Dubremetz, S. Fauquenoy, S. Tomavo, B.W. Faber, C.H. Kocken, A.W. Thomas, M.J.
598        Boulanger, G.A. Bentley, and M. Lebrun. 2011. The RON2-AMA1 interaction is a critical step
599        in moving junction-dependent invasion by apicomplexan parasites. *PLoS Pathog*.
600        7:e1001276. doi:10.1371/journal.ppat.1001276.

601   Marino, N.D., M.W. Panas, M. Franco, T.C. Theisen, A. Naor, S. Rastogi, K.R. Buchholz, H.A. Lorenzi,
602        and J.C. Boothroyd. 2018. Identification of a novel protein complex essential for effector
603        translocation across the parasitophorous vacuole membrane of Toxoplasma gondii. *PLoS*
604        *Pathog*. 14:e1006828. doi:10.1371/journal.ppat.1006828.

605   Monteiro, V.G., E.J. de Melo, M. Attias, and W. de Souza. 2001. Morphological changes during
606        conoid extrusion in Toxoplasma gondii tachyzoites treated with calcium ionophore. *J Struct*
607        *Biol*. 136:181–189. doi:10.1006/jsbi.2002.4444.

608   Mordue, D.G., N. Desai, M. Dustin, and L.D. Sibley. 1999. Invasion by Toxoplasma gondii establishes a
609        moving junction that selectively excludes host cell plasma membrane proteins on the basis
610        of their membrane anchoring. *J Exp Med*. 190:1783–1792. doi:10.1084/jem.190.12.1783.

611   Morrissette, N.S., and L.D. Sibley. 2002. Cytoskeleton of apicomplexan parasites. *Microbiol Mol Biol*
612        *Rev*. 66:21–38; table of contents. doi:10.1128/mmbr.66.1.21-38.2002.

613   Nichols, B.A., and M.L. Chiappino. 1987. Cytoskeleton of Toxoplasma gondii. *J Protozool*. 34:217–
614        226. doi:10.1111/j.1550-7408.1987.tb03162.x.

615     Nichols, B.A., M.L. Chiappino, and G.R. O'Connor. 1983. Secretion from the rhoptries of Toxoplasma
616             gondii during host-cell invasion. *J Ultrastruct Res*. 83:85–98. doi:10.1016/s0022-
617             5320(83)90067-9.

618     Paredes-Santos, T.C., W. de Souza, and M. Attias. 2012. Dynamics and 3D organization of secretory
619             organelles of Toxoplasma gondii. *J Struct Biol*. 177:420–430. doi:10.1016/j.jsb.2011.11.028.

620     Pastor-Fernández, I., S. Kim, V. Marugán-Hernández, F. Soutter, F.M. Tomley, and D.P. Blake. 2020.
621             Vaccination with transgenic Eimeria tenella expressing Eimeria maxima AMA1 and IMP1
622             confers partial protection against high-level E. maxima challenge in a broiler model of
623             coccidiosis. *Parasit Vectors*. 13:343. doi:10.1186/s13071-020-04210-2.

624     Saffer, L.D., O. Mercereau-Puijalon, J.F. Dubremetz, and J.D. Schwartzman. 1992. Localization of a
625             Toxoplasma gondii rhoptry protein by immunoelectron microscopy during and after host cell
626             penetration. *The Journal of protozoology*. 39:526–530.

627     Scholtyseck, E., and H. Mehlhorn. 1970. Ultrastructural study of characteristic organelles (paired
628             organelles, micronemes, micropores) of sporozoa and related organisms. *Z Parasitenkd*.
629             34:97–127. doi:10.1007/BF00260383.

630     Shirley, M.W., and D.A. Harvey. 1996. Eimeria tenella: infection with a single sporocyst gives a clonal
631             population. *Parasitology*. 112 ( Pt 6):523–528. doi:10.1017/s0031182000066099.

632     Suarez, C., G. Lentini, R. Ramaswamy, M. Maynadier, E. Aquilini, L. Berry-Sterkers, M. Cipriano, A.L.
633             Chen, P. Bradley, B. Striepen, M.J. Boulanger, and M. Lebrun. 2019. A lipid-binding protein
634             mediates rhoptry discharge and invasion in Plasmodium falciparum and Toxoplasma gondii
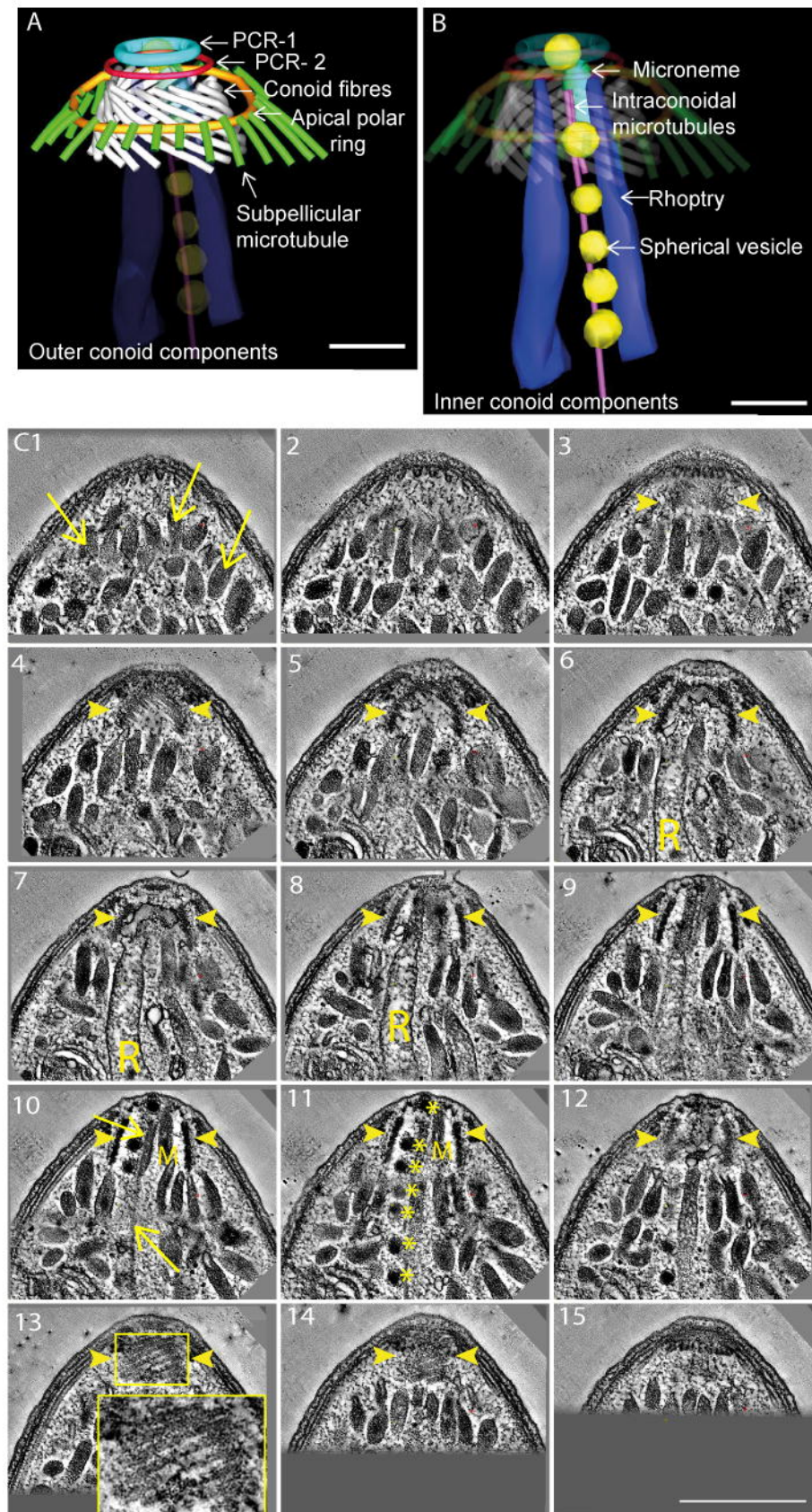635             parasites. *Nat Commun*. 10:4041. doi:10.1038/s41467-019-11979-z.
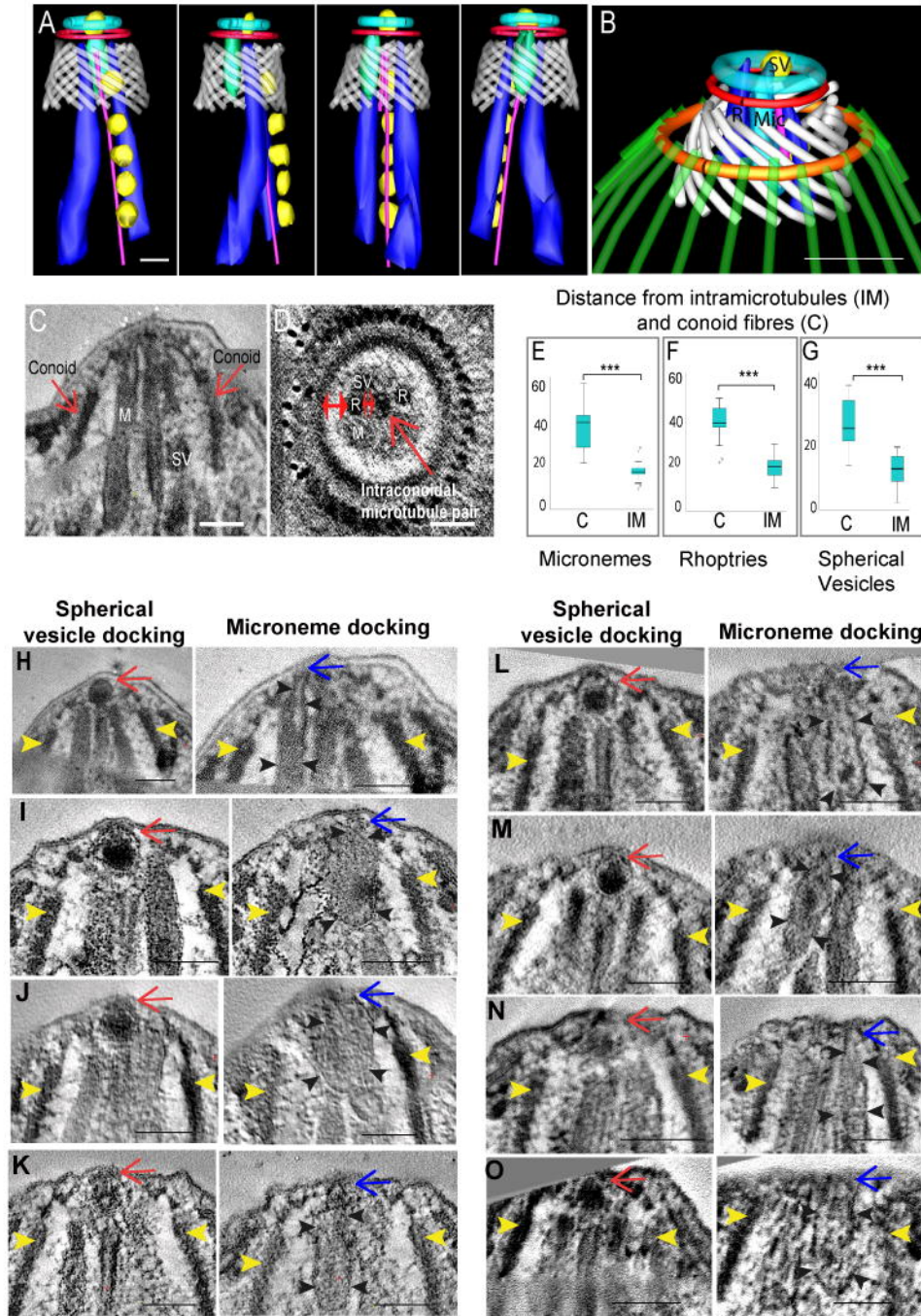
636

# figure 1

# Figure 2

# Figure 3

# Figure 4



A. Micronemes, Rhoptry, Acidocalcisome, Anterior refractile body, Nucleus, Mitochondria, Amylopectin granules, Posterior refractile body

B. Rhoptry, Micronemes

C. Mitochondria, Nucleus

D. micronemes

E. rhoptries

F.

G.
- cytoplasm/other 48%
- Nucleus 5%
- Refractile bodies 36%
- Amylopectin granules 4%
- Mitochondria 2%
- Acidocalcisomes 1%
- Micronemes 5%
- Rhoptries 1%

cytoplasm/other 48%
Refractile bodies 36%